JCTC Journal of Chemical Theory and Computation

Article

The role of core electrons in quantum dynamics using TDDFT

Nicolas Oscar Foglia, Uriel N. Morzan, Dario A Estrin,
Damian A. Scherlis, and Mariano Camilo Gonzalez Lebrero

J. Chem. Theory Comput., **Just Accepted Manuscript** • DOI: 10.1021/acs.jctc.6b00771 • Publication Date (Web): 22 Nov 2016

ACS Publications

Journal of Chemical Theory and Computation is published by the American Chemical Society. 1155 Sixteenth Street N.W., Washington, DC 20036

The role of core electrons in quantum dynamics using TDDFT

Nicolás O. Foglia,[†] Uriel N. Morzan,[†] Dario A. Estrin,[‡] Damian A. Scherlis,[*,†] and Mariano C. Gonzalez Lebrero[*,†]

[†]*Departamento de Química Inorgánica, Analítica y Química Física/INQUIMAE, Facultad de Ciencias Exactas y Naturales, Universidad de Buenos Aires, Ciudad Universitaria, Pab. II, Buenos Aires (C1428EHA) Argentina*

[‡]*Departamento de Química Inorgánica, Analítica y Química Física/INQUIMAE-CONICET, Facultad de Ciencias Exactas y Naturales, Universidad de Buenos Aires, Ciudad Universitaria, Pab. II, Buenos Aires (C1428EHA) Argentina*

E-mail: damian@qi.fcen.uba.ar; nanolebrero@qi.fcen.uba.ar

Abstract

The explicit simulation of time dependent electronic processes requires computationally onerous routes involving the temporal integration of motion equations for the charge density. Efficiency optimization of these methods typically relies on increasing the integration time-step and on the reduction of the computational cost per step. The implicit representation of inner electrons by effective core potentials—or pseudopotentials—is a standard practice in localized-basis quantum-chemistry implementations to improve the efficiency of ground state-calculations, still preserving the quality of the output. This article presents an investigation on the impact that effective core potentials have on the overall efficiency of real time electron dynamics with TDDFT. Interestingly, the speedups achieved with the use of pseudopotentials in this

kind of simulations are on average much more significant than in ground-state calculations, reaching in some cases a factor as large as 600×. This boost in performance originates from two contributions: on the one hand, the size of the density matrix, which is considerably reduced; and on the other, the elimination of high-frequency electronic modes, responsible for limiting the maximum time-step, which vanish when the core electrons are not propagated explicitly. The latter circumstance allows for significant increases in time-step, that in certain cases may reach up to three orders of magnitude, without loosing any relevant chemical or spectroscopic information.

1 Introduction

Many fundamental processes of general relevance in nature and technology, from the respiratory chain to the photo-luminescence of light-emitting diodes, involve the dynamics of electrons in molecules, nanostructures, and mesoscopic systems.[1–5] This has motivated the proliferation of theoretical methods aimed to solve the quantum many-body problem in the time-domain. In the context of *ab-initio* methods, time-dependent density functional theory (TDDFT)[6] has become the most popular approach, with a success relying on an extraordinary balance between predictive power and computational efficiency. While the vast majority of existing TDDFT implementations are based on a perturbative strategy within linear-response theory (LR-TDDFT), the simulation of quantum-dynamics in processes as those mentioned above, or in the interaction with intense external fields, may require the explicit time-domain propagation of the Kohn-Sham equations. To this end, in recent years implementations designed to evolve the Kohn-Sham states in real time (RT-TDDFT) have started to emerge.[7–12] These implementations are based on numerical integration of the electronic equations of motion, assuming a finite time-step which is typically two to three orders of magnitude smaller than a femtosecond. At every step, all terms of the Kohn-Sham matrix have to be recalculated. Thus, simulations evolving for 10 or 20 femtoseconds may become very costly and even unfeasible for systems of a few hundreds of electrons.

It is well known that most of chemistry is determined by the valence charge density, with the core electrons remaining essentially undisturbed relative to their distribution in isolated atoms in the majority of the processes of interest to chemists. This circumstance has led to the formulation of a variety of ab-initio electronic structure models which, to gain computational efficiency, avoid the explicit description of the inner electrons, and compensate for their effect on the valence density with additional potentials added to the Hamiltonian.[13,14] Such potentials are known as pseudopotentials, or effective core potentials (ECP)[15] in the realm of Gaussian basis sets implementations. The advantage of ECP methods is twofold: on the one hand they reduce the size of the basis set required to correctly represent the elec-

tronic structure; and on the other hand they offer a route to introduce relativistic corrections in heavy atoms.

Real-time time-dependent density functional implementations have been developed both in the plane-waves (PW) and localized basis sets frameworks. In the implementations of the first kind, such as CPMD,[10,16] the representation of core electrons is computationally very demanding and the adoption of pseudopotentials is the rule. Whereas PW schemes are naturally suited for periodic structures, localized basis methods have been devised in both periodic and non-periodic boundary conditions. Gaussian functions are the most common type of localized basis employed in the context of real time TDDFT simulations,[7–9,17] but in general they are limited to finite systems in open-boundaries. On the other hand, they offer the possibility to perform calculations with hybrid DFT functionals at a very affordable cost in comparison with a PW setting, in which the computation of the exact exchange matrix turns out to be much more expensive. There are other real time TDDFT schemes capable of dealing with periodic boundary conditions using localized basis-sets. The SIESTA method uses numerical basis but provides a periodic description of the density and the potential thanks to the use of a real space grid and a Fourier-space representation.[18,19] The GPAW program combines PW and atom-centered basis, being able to solve the electronic structure either in periodic or open-boundary conditions.[20] This capability is shared by the Octopus code, which does not rely on basis-functions but solves the electronic problem directly on a real space grid.[21] Some of the most interesting physical-chemical processes, as for example those mentioned at the beginning of this introduction, occur in the condensed phase, or in complex environments. In these cases the periodic schemes implemented in Octopus, CPMD or GPAW codes represent an advantage. The implementation described in the present article is not periodic, but can deal with these situations by means of a multi scale QM-MM strategy (see references[22] and[23]).

Different approaches have been used to integrate the equations of motion for the electrons, including the Magnus, the Crank-Nicholson, and the split-operator techniques, among several

others.[24] In some cases these schemes have been merged for improved results. For example, Sugino and Miyamoto have combined a higher-order Suzuki-Trotter type split operator with a cutoff of the kinetic and potential energy operators, and the replacement of the usual predictor-corrector approach by the so-called "railway curve interpolation" to update the self-consistent potential. With this strategy they substantially improved the numerical stability of the propagation, reaching an increase in the time-step of at least an order of magnitude. This technique has been adopted in some recent PW implementations.[25] As explained below (section 2.2), in the present paper we employ a simpler propagator.

In this work, we show than in a RT-TDDFT scheme, the incorporation of pseudopotentials offers an additional substantial advantage: aside from the impact on the dimension of the density matrix, which may significantly alleviate the cost of the propagation algorithm, it also extends the length of the required time-step, by eliminating the need to integrate the motion of the inner electrons, associated with high energy transitions and fast fluctuation frequencies. In what follows, we analyze the effects of pseudopotentials on time-step, stability and efficiency of RT-TDDFT. We choose the absorption energies associated with the electronic spectrum as a quality parameter for comparison with other approaches like LR-TDDFT or all-electron calculations. The remainder of this paper takes the following form: the overall methodology is outlined in section 2, where the general SCF process and initial electronic structure is discussed in section 2.1, the propagation scheme is detailed in 2.2, section 2.3 explains the strategy to obtain absorption spectra, and section 2.4 highlights the basics aspects concerning the implementation of ECP. The contributions of core and valence electrons during time propagation are analyzed in section 3.1, section 3.2 explores the stability of electron dynamics and, finally, the effect of pseudopotential on electron dynamics is studied in section 3.3.

2 Methodology

2.1 General details

All RT-TDDFT calculations reported in this study have been performed with the LIO code, developed in our group.[22,23] The LIO project encompasses a highly efficient DFT program based on Gaussian functions, which uses radial grids to compute the exchange-correlation energy, and handles the most expensive parts of the calculation in graphic processing units (GPUs). All the simulations reported in this study were performed using the Perdew-Burke-Ernzerhof (PBE) generalized gradient approximation functional.[26,27]

The total energy in DFT is expressed as a sum of the terms in eq. 1, where T_s corresponds to the kinetic energy of the electrons, V_{Ne} to the interaction between nuclei and electrons, V_{ee} to the electronic repulsion, and E_{XC} to the exchange-correlation contribution.

$$E[\rho] = T_s[\rho] + V_{Ne}[\rho] + V_{ee}[\rho] + E_{XC}[\rho] \tag{1}$$

To generate the initial state in electron dynamics simulations, the system is usually relaxed to its ground state and then subjected to an external perturbation which moves it away from equilibrium.

2.2 Time evolution

Absorption spectra and other dynamical properties can be obtained from the temporal evolution of the electron density. In particular the electronic absorption spectrum can be computed from the response of the dipole moment after the application of an external electric field (see section 2.3). The dynamics can be propagated in terms of the density matrix $\overline{\overline{P}}$ according to the Liouville-von Neumann equation (hereafter, a single bar on top of an object will denote a vector, and a double bar a matrix):

$$i\hbar\frac{\partial\overline{\overline{P}}}{\partial t} = [\overline{\overline{H}}, \overline{\overline{P}}] \tag{2}$$

where $\overline{\overline{H}}$ is the matrix associated with the electronic Hamiltonian, and $\overline{\overline{P}}$ is expressed in the orthogonal basis of the molecular orbitals $\psi_i(\overline{r}, t)$,

$$\psi_i(\overline{r}, t) = \sum_{\mu=1}^{N_{AO}} C_{\mu i}(t)\phi_\mu(\overline{r}), \tag{3}$$

$$P_{\mu\nu} = \sum_{i=1}^{N_{MO}} C^*_{\mu i}(t)C_{\nu i}(t). \tag{4}$$

$\phi_\mu(\overline{r})$ is an element of the atomic basis set of size N_{AO}, and N_{MO} is the number of occupied molecular orbitals.

Different algorithms have been proposed to integrate the electron dynamics in eq. 2. In the LIO code two routes have been implemented: a Verlet scheme[23] which provides a simple expression for the temporal evolution; and a more complex algorithm based on the Magnus expansion,[17] requiring the calculation of a greater amount of commutators, but with the advantage of tolerating significantly longer time-steps.[23] In this paper we used the Verlet propagator because, given its simplicity and its higher sensitivity to the time-step, it offers a more suitable test-bed to examine the stability of the dynamics. According to this integration scheme the electron density at time $t + \Delta t$ is computed by this simple formula:

$$\overline{\overline{P}}(t + \Delta t) = \frac{2}{i\hbar}[\overline{\overline{H}}(t), \overline{\overline{P}}(t)]\Delta t + \overline{\overline{P}}(t - \Delta t). \tag{5}$$

2.3 Absorption spectra calculations

As in previous publications,[23,28] absorption spectra were obtained from the response of the electronic system to a narrow linearly polarized gaussian electric field ($\overline{E}(t)$) resembling the effect of a time domain δ function kick, which excites all the resonances with the same

intensity:

$$\overline{E}(t) = E_0 \cdot \exp[-(t-t_0)^2/2\omega^2]\hat{r} \tag{6}$$

where t_0 is the time at which the pulse reaches its maximum value E_0, ω is its width, and $\hat{r}$ is the unitary vector pointing in the direction of x, y or z. Within this work, E_0 and ω were fixed, respectively, to 10^{-3} atomic units (au, 1 au = 0.002419 fs) and $\frac{\sqrt{10}}{2}\Delta t$ (with Δt the integration time-step). The applied field enters the Hamiltonian through its coupling with the electric dipole moment,

$$V_{app}(t) = -\overline{E}(t) \cdot \overline{\mu}(t). \tag{7}$$

The absorption spectrum $S(\omega)$ is calculated from the the absorption cross section tensor $\overline{\overline{\sigma}}(\omega)$,

$$S(\omega) = \frac{1}{3} Tr[\overline{\overline{\sigma}}(\omega)], \tag{8}$$

$$\overline{\overline{\sigma}}(\omega) = \frac{4\pi\omega}{c} Im[\overline{\overline{\alpha}}(\omega)], \tag{9}$$

where $\overline{\overline{\alpha}}$ is the linear polarizability tensor. To compute $\overline{\overline{\alpha}}$ from a time-dependent simulation, we consider the following first order expansion for the dipole moment:

$$\mu_{ik}(t) = \mu_k^o + \int dt_1 \alpha_{ik}(t-t_1) E_i(t_1) = \mu_{ik}^o + \mu_{ik}^{ind}(t). \tag{10}$$

In this equation, μ_k^o is the $\hat{k}$ component of the electric dipole in the absence of an external perturbation, and the index i indicates the direction of the applied field (every spectrum is obtained from three simulations, in each of which the perturbation is applied along the x, y, and z directions). Rewriting eq. 10 in the frequency domain, the polarizability tensor can

be expressed as a function of the induced dipole $\mu^{ind}(t)$ obtained from the dynamics:

$$\alpha_{ik}(\omega) = \frac{\mu_{ik}^{ind}(\omega)}{E_i(\omega)} = \frac{\int dt\ e^{i\omega t}\mu_{ik}^{ind}(t)e^{-\gamma t}}{\int dt\ e^{i\omega t}E_i(t)}. \tag{11}$$

The damping factor $e^{-\gamma t}$ is added to the expression above to produce a broadening in the absorption spectrum peaks emulating the coupling effects between electronic and nuclear degrees of freedom. Within this work values in the order of 0.1 au were adopted.

2.4 Effective Core Potentials

The ECP are terms included in the Hamiltonian, to mimic the interaction between the (absent) inner electrons and the valence charge, restraining the penetration of the latter in the nuclear region. As already mentioned, the advantage of pseudopotentials is, on the one hand, to reduce the size of the basis set and therefore the dimension of the matrices involved in the calculation, and, on the other hand, to parametrize relativistic corrections. In Gaussian basis methods, the contribution of an atomic pseudopotential to the total Hamiltonian is given by the following equation:[15]

$$V^{core}(r) = V_{LMAX} + \sum_{l=0}^{LMAX-1}\sum_{m=-l}^{l} |l,m\rangle\Big(V_l(r) - V_{LMAX}(r)\Big)\langle l,m| \tag{12}$$

where r is the distance to the atom center, $V_l(r)$ are radial functions usually parametrized as a product of Gaussian and polynomials functions, and $|l,m\rangle$ are real orthonormal spherical harmonics centered on the atom. To construct $V_l(r)$ some ad hoc decisions must be made, such as the maximum angular momentum to be included in the parametrization (LMAX), the boundary of the core region, and the particular relativistic approach. These variants have led to different families of pseudopotentials. The Compact Effective Potential "CEP"[29–31] (also denoted by the acronym SBKJC), the CRENBL,[32–35] the Los Alamos,[36–38] and the Stuttgart[39] pseudopotentials, are examples of common parametrizations employed

with Gaussian basis. In this article the CEP scheme was adopted, because, being constructed with a small number of functions, it proved to be the most efficient within our code, without prejudice to the quality of the results. In any case, additional tests were performed with different ECP for comparison, which results are presented as supporting information.

The present ECP implementation in the LIO program follows the work by Bode and Gordon[40] for all integrations, though we introduce a cut-off distance (R_{cutoff}) so that the computational cost scales linearly with the system size. Thus, the interaction between the electrons and a pseudopotential centered on atom I, is restrained by the condition $\alpha_i|\overline{MI}|^2 < R_{cutoff}$, where $|\overline{MI}|$ is the distance between the origin of the basis function M and atom I, with α_i the basis exponent. Appropriate cut-off radii were determined from energy calculations in different systems.

3 Results and Discussion

3.1 Split propagation of $\overline{\overline{P}}$

The treatment in section 2.3 provides a route to the electronic frequencies from the evolution of the total charge density. In this study, however, we seek to individualize the contribution of every orbital to the absorption spectrum, to analyze separately the role of core and valence electrons. This can be achieved by propagating the TDDFT equations in terms of the Kohn-Sham orbitals. alternatively, this can also be accomplished using the Liouville von Neumann master equation (eq. 2), providing the density matrix is decomposed in N_{MO} matrices $\overline{\overline{P^i}}$, which elements consist of a single term of the sum in eq. 4:

$$P^i_{\mu\nu}(t) = C^*_{\mu i}(t)C_{\nu i}(t). \tag{13}$$

In the electronic ground state, every matrix $\overline{\overline{P^i}}$ is associated with the Kohn-Sham orbital i. Thanks to the linearity of all operations when integrating via eq. 5, it is possible to evolve

each matrix $\overline{\overline{P^i}}$ separately; this set of equations, however, is coupled because $\overline{\overline{H}}$ depends on the total electron density of the system. The above decomposition is schematized in Figure 1.

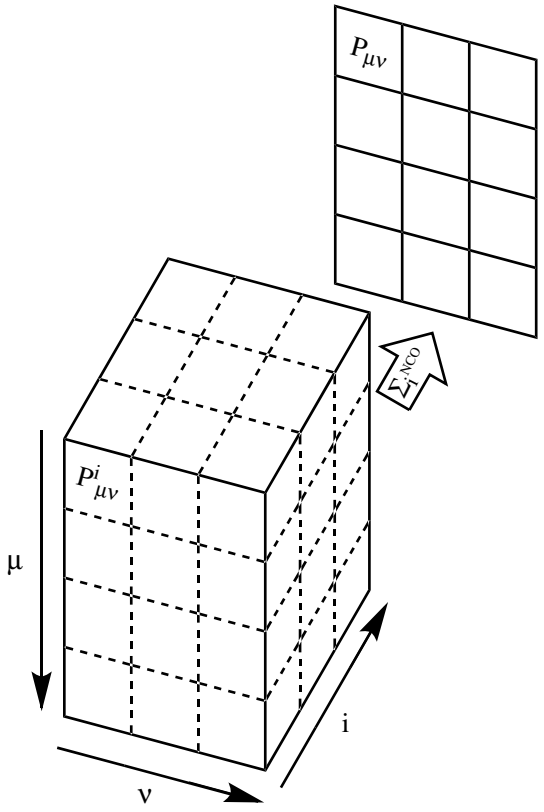

Figure 1: To track the contribution of every molecular orbital to the frequency spectrum, the density matrix is decomposed in N_{MO} matrices $\overline{\overline{P^i}}$. Each of these is evolved separately, reflecting the dynamics of the ith molecular orbital.

The HCl molecule was chosen to test the behavior of this split propagation scheme, because it is small but has enough electrons for the ECP to make a difference in performance, and to establish a clear distinction between core and valence charge. For small systems as those considered here, linear response schemes are likely to be computationally less demanding to access absorption spectra with respect to a real time approach; in the present work, however, the interest is not to obtain the electronic spectrum, but to employ it as a quality-test of the dynamics. In its low energy region, the experimental absorption spectrum of HCl

presents a band centered at $\sim 8\ eV$,[41,42] which will be used to benchmark our calculations. To calculate the spectrum the system must be subjected to three orthogonal perturbations, and its response needs to be computed in each case. However, to the end of this study, which aims at examining the role of core electrons on the simulated dynamics, it would be irrelevant to impose the excitations in all directions to extract the full spectrum. Instead, it is enough to reproduce the response of the system to the perturbation in some axis, since the quantity of interest is basically the maximum time-step, and the overall computation time. Excitations in the three axes would involve additional complexity, providing no further insight. Thus, to keep the analysis simple, we have focused on one of the three contributions to the absorption spectra. As shown in Figure 2, the generalization to the other axes does not affect the comparison.

Figure 2 shows the resulting spectra for HCl, displaying also the contributions of each diagonal element of the absorption cross section tensor $\overline{\overline{\sigma}}$ (which reflects the imaginary part of the polarizability tensor). In our analysis, we will consider the components of $\overline{\overline{\sigma}}$ perpendicular to the molecular axis, because they are responsible for the transition of interest in the low energy range of the spectrum.

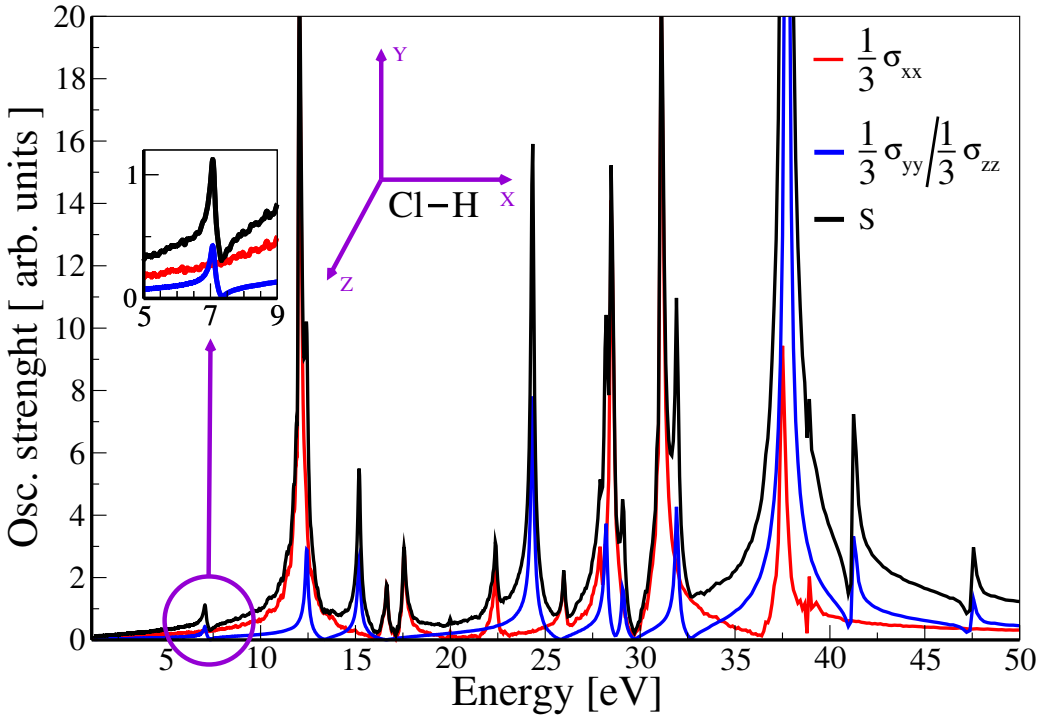

Figure 2: Absorption spectrum, and individual contributions of the absorption cross section tensor, calculated for the HCl molecule. Given the orientation of the molecule, the yy and zz elements are equivalent. Every spectrum has been computed from simulations of 50 fs using a 6-311G** basis set and a time-step of 0.001 au.

The left panel in Figure 3 shows the frequencies of the HCl molecule obtained with a 6-311G** basis set,[43,44] for an applied electric field perpendicular to the molecular axis. Given the total number of electrons, and assuming a closed-shell representation, there are 9 $\overline{\overline{P^i}}$ matrices to be propagated, each one associated with a particular ground state molecular orbital. We note that $\overline{\overline{P^1}}$ and $\overline{\overline{P^2}}$ are essentially related to orbitals 1s and 2s of Cl, respectively, whereas $\overline{\overline{P^3}}$ to $\overline{\overline{P^5}}$ can be identified with the 2p electrons of Cl. The absorption spectrum arises from the full density matrix computed from the sum of all the propagated matrices. The contribution of the 5 orbitals associated with the lower eigenvalues in the ground state, were grouped as part of the "core" frequencies, while that of the remaining orbitals were considered "valence". The right panel depicts the dipole moment (in the direction of the perturbation) calculated from the charge density of selected orbitals. It is manifest that the

dipole moment associated with the evolution of the lower energy orbitals, for example 1, fluctuates much faster than in the case of the higher energy electrons, for example 3 or 9. This behavior is reflected in the fact that the major contribution to the lower part of the absorption spectrum originates from the valence electrons.

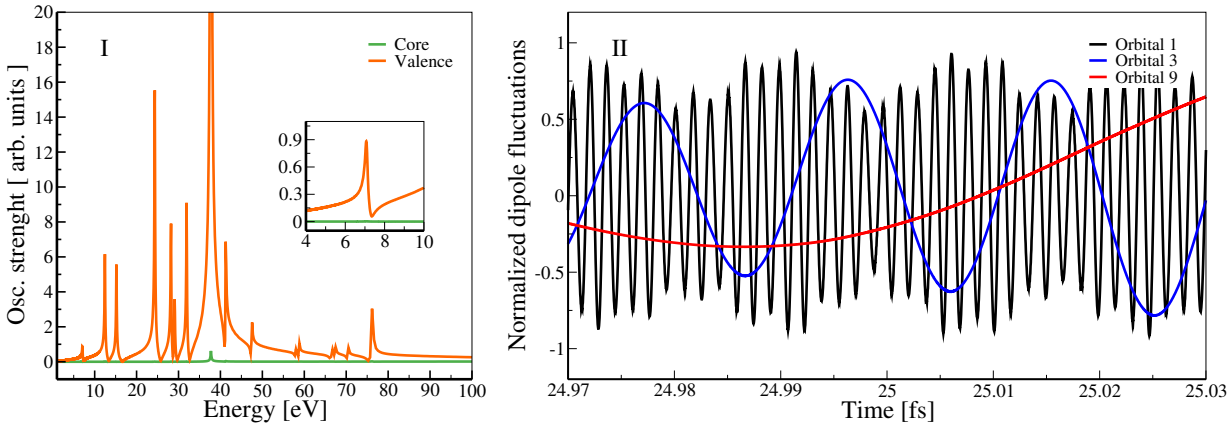

Figure 3: (I) Oscillator strength calculated for the HCl molecule from the split-propagation scheme (see text, section 3.1). The contribution of the core states is depicted in green and that of the valence charge in orange. The inset zooms on the transition of interest. (II) Temporal evolution of the dipole moment (in the direction of the perturbation) associated with selected orbitals. The calculation corresponds to a 50 fs simulation using a 6-311G** basis set and a time step of 0.001 au.

It is well known that the optimal time-step to integrate any dynamical equation is determined by the highest frequency in the system. This example clearly shows than in electron dynamics, the faster fluctuations are related to the first eigenstates, or, in other words, that core electrons are the limiting factor in the length of the time-step. We focus on this question in the next section.

3.2 Propagator stability

According to the Liouville von Neumann equation (eq. 2) the variation rate of the density matrix is given by the commutator $[\overline{\overline{H}}(t), \overline{\overline{P^i}}(t)]$. Usually, the loss of stability in the propagation algorithm is manifested in the divergence of the density matrix, and therefore of

its commutator with the time-dependent Hamiltonian. In order to analyze the stability of the electron dynamics and its dependence on the time-step, the norms of the commutators were followed along the split propagation. Figure 4 shows the results for 5000 steps of dynamics using different time-steps, for molecular orbitals 1 (black) and 9 (red), which are the most internal and external, respectively. It can be seen that fluctuations in the commutator norm are much more sensitive to the time-step for orbital 1 in comparison to orbital 9. In particular, there is a limiting time-step ($\sim$0.00315 au), which will be referred to as T_{max}, above which the commutator diverges before completing 5000 steps. For this time-step the propagation of orbital 9 necessarily diverges as well, with some delay, since all electronic modes are coupled through the Hamiltonian matrix in the commutator. The distinctive sensitivity to time-step of these fluctuations, suggests that T_{max} is too high to propagate the lower eigenstates, whereas it appears appropriate to integrate the lower frequency modes. To further assess the incidence of the inner electrons on the time-step, the same analysis was repeated for a partially frozen-core configuration, i.e., performing the propagation without evolving the $\overline{\overline{P^1}}$ matrix. The bottom panel on the right in Figure 4 presents the results corresponding to using T_{max}: the propagation does not diverge within the first 5000 steps, and the oscillations in the norm of the commutator associated with the valence orbital become much smoother.

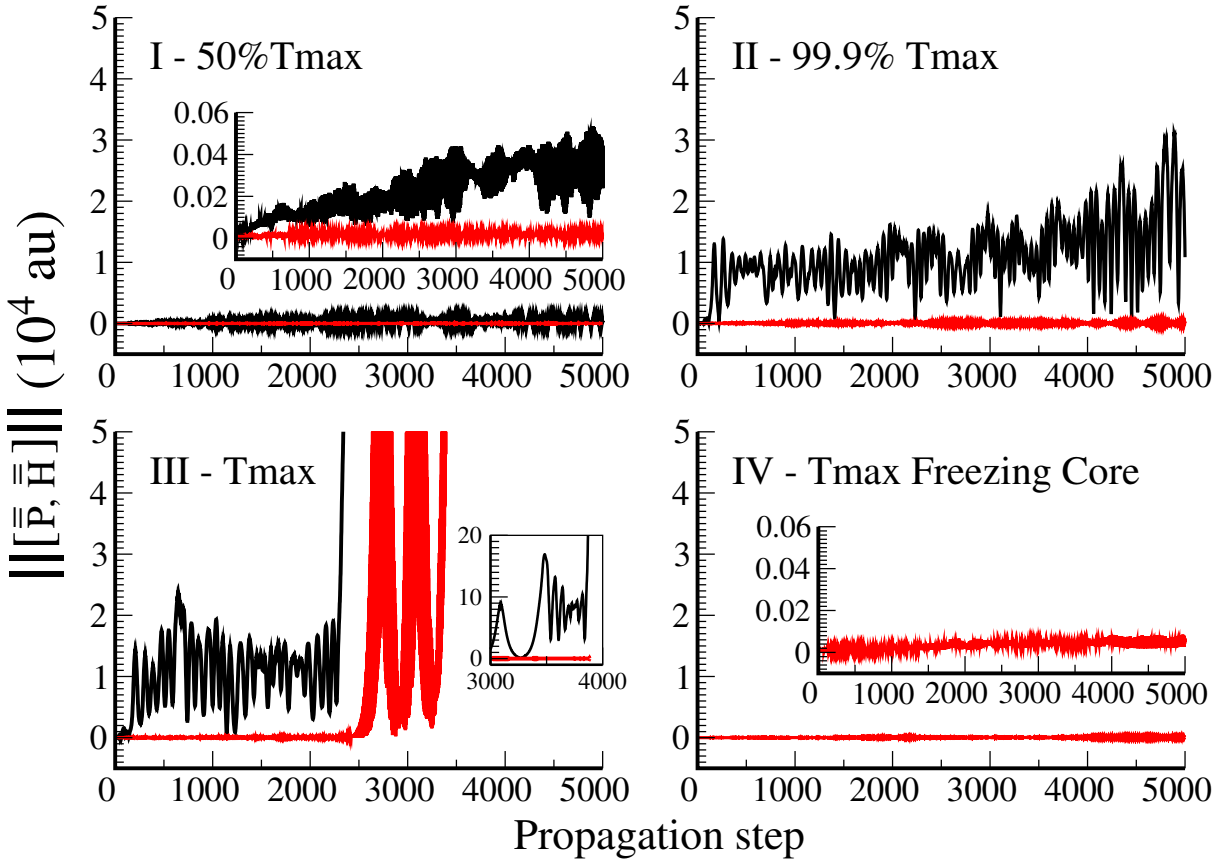

Figure 4: Temporal evolution of the norm of $[\overline{\overline{H}}(t), \overline{\overline{P^i}}(t)]$ (in atomic units) for molecular orbitals i=1 (black) and i=9 (red) during the simulation of the HCl molecule, using the Verlet propagator with different integration time-steps. Panels I, II, and III show, respectively, results obtained from time-steps equivalent to 50%, 99%, and 100% of Tmax (maximum tolerated time-step, ∼0.00315 au). Finally Panel IV displays the magnitude of $[\overline{\overline{H}}(t), \overline{\overline{P^9}}(t)]$ when freezing the $\overline{\overline{P^1}}$ matrix and integrating with a time-step of Tmax. A 6-311G** basis set was used for all calculations.

The effect of freezing the core orbitals on the absorption spectrum is considered in Figure 5. It can be seen that the low energy region is essentially independent of the evolution of the inner electrons, even when the full core charge—the set of the first five orbitals—is frozen. At least for HCl, these results show that the dynamics of the core electrons does not modify the absorption spectrum in the low energy range, which is the one of general interest. Therefore, the use of ECP in the time-propagation should allow for more efficient electron dynamics without loss of relevant spectroscopic information with respect to the all-electron calculation.

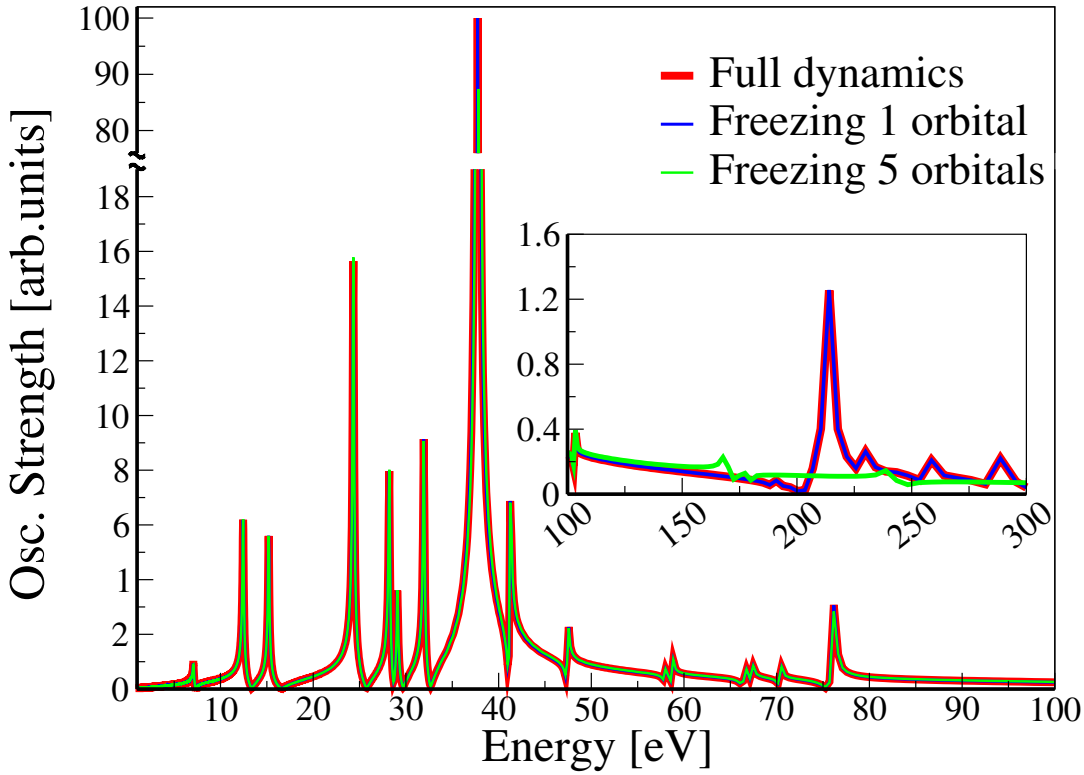

Figure 5: Oscillator strength calculated for the HCl molecule. Results for all-electron dynamics (red), and frozen-core dynamics, freezing the lowest-energy orbital (blue), and the set of 5 lower-energy orbitals (green). The inset presents the high-energy region, in eV. Spectra were computed from 50 fs simulations using a time-step of 0.001 au and a 6-311G** basis set.

3.3 RT-TDDFT using ECP

The implementation of a pseudopotential scheme in the framework of Gaussian basis methods requires the parametrization of a specific basis set to represent the valence orbitals in the presence of a given core potential. In this way, each set of pseudopotentials has an associated set of basis functions designed to optimize its performance for SCF calculations. Most of the basis sets designed for ECP, are typically constructed to reproduce ground state properties. However, TDDFT calculations are meant to represent both ground and excited states, and the computed absorption frequencies usually turn out to be very sensitive to the choice of basis functions. In particular, the spectrum computed with the 6-311G**

basis[43,44] from an all-electron simulation exhibits significant differences with respect to that obtained from a CEP pseudopotential[29] calculation (data not shown). Even if the CEP basis is augmented with polarization functions,[45,46] the frequencies continue to differ significantly from those emerging from the calculation with the 6-311G** basis set. Therefore, for the sake of comparison, in the pseudopotential calculations we have replaced the specific CEP basis by the same 6-311G** functions used in the all-electron runs. This fusion will be denoted as ECP/6-311G**. Alternatively, we have also explored the same combination but removing the innermost functions of the 6-311G** basis, which will be referred to as ECP/6-311G** (valence only).

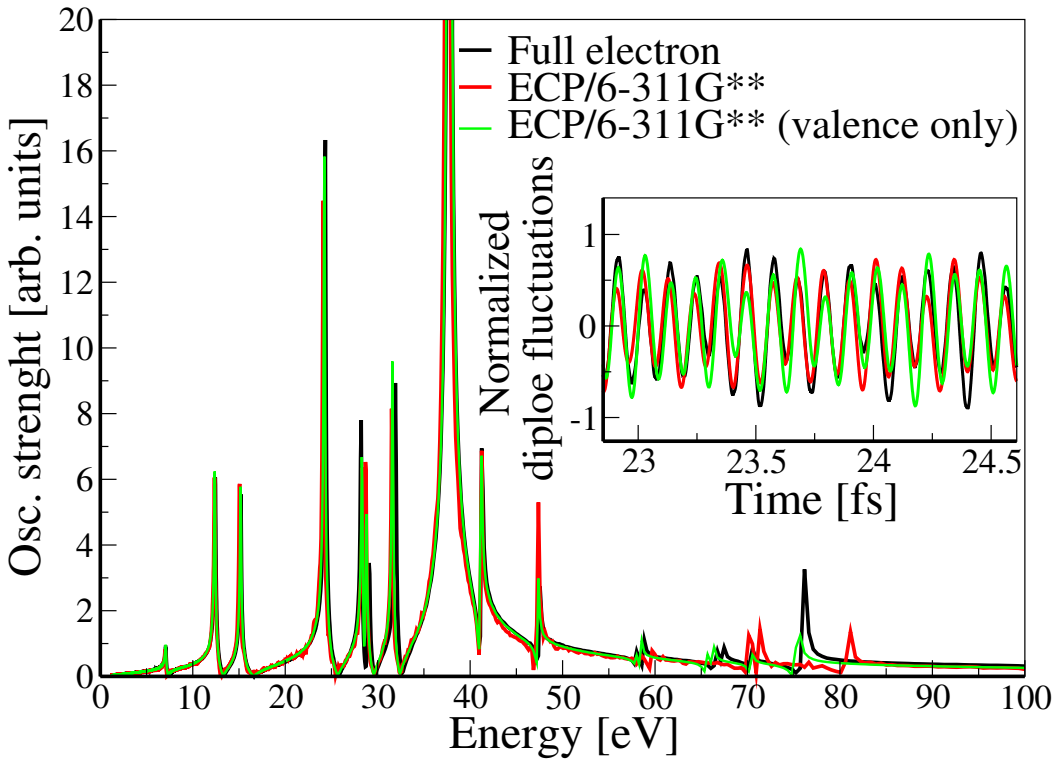

Figure 6: Oscillator strength calculated for the HCl molecule using the 6-311G** basis set, obtained from the all-electron (black) and CEP simulations in combination with the 6-311G** basis set, with and without the core functions (red and green respectively). The corresponding time-dependent dipole moments are displayed in the inset.

Figure 6 compares all-electron (black curve) and CEP calculations (red curve), performed

in every case with the full 6-311G** basis set,[43,44] for the absorption of the HCl molecule. The agreement suggests that the aforementioned differences in the frequencies emerging from CEP and all-electron 6-311G** calculations are not related to the core representation, but their origin can be attributed to the basis set quality. If the innermost functions of the 6-311G** basis set are removed to give the ECP/6-311G** (valence only) basis, green curve in Figure 6, the low energy part of the spectrum obtained from time-dependent calculations is analogous to the corresponding spectra calculated with the full basis set. As already seen in the previous results, this region is practically unaffected by the use of the effective core potentials.

Even though the accuracy in the low energy range is about the same for the all-electron and pseudopotential calculations, the computational cost differs almost by an order of magnitude. The maximum time-step allowing for stable integration turns out to be ∼0.015 au and ∼0.003 au for the ECP/6-311G** (valence only) and the all-electron simulations, respectively. The overall gain in efficiency, of about 10×, is not explained by the sole time-step increment (of 5×) but also from the faster computation of the Kohn-Sham and density matrices with the smaller basis set associated with ECP.

Figure 7 depicts the values of T_{max} in all-electron/DZVP[46,47] and CEP pseudopotentials dynamics, for alkaline earth metals, halides, and binary species of carbon. We recall that this value corresponds to the longer time-step allowing for the stable integration of equation of motion 5 along 5000 steps of dynamics. In the all-electron calculations, T_{max} decreases rapidly when going down within a given Group in the Periodic Table. This is the expected trend with the increase of the atomic charge, which rises the frequencies associated with the inner electrons. The Figure shows that this trend on time-steps is effectively neutralized with the use of core potentials.

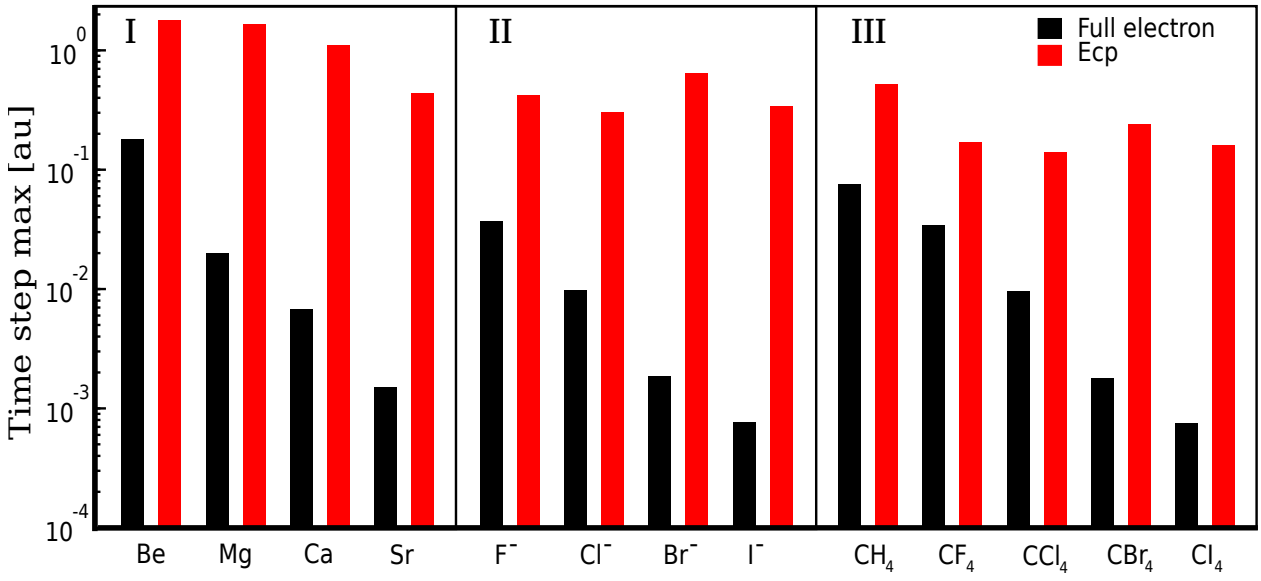

Figure 7: Maximum time-steps tolerated in electron dynamics simulations using the Verlet propagator. Full electron and ECP calculations were performed with DZVP and CEP basis sets, respectively. (I) alkaline earth metals. (II): halides. (III): carbon binary species.

As already mentioned, the improvement in the efficiency of pseudopotential-based electron dynamics stems not only from higher time-steps, but also, of course, from a reduction of the dimension of the matrices $\overline{\overline{H}}$ and $\overline{\overline{P}}$. The main operations involved in the Liouville-von Neumann propagation, i.e., matrix multiplications and the calculation of the Kohn-Sham operator, scale cubic with the size of these matrices. Table 1 shows for various systems, the total simulation times elapsed in an hour of execution in a NVIDIA GeForce GTX 760 GPU in combination with an Intel Core i5-4430 CPU.

Table 1: Electron dynamics simulation times (femtoseconds) accomplished in one hour of execution in a GTX 760 GPU. Full-electron and ECP calculations were performed with DZVP and CEP basis sets, respectively.

	ECP		Full-electron		
System	$T_{max}(au)$	(fs/h)	T_{max} (au)	(fs/h)	Speedup
Be	1.8	40645.88	0.18	3730.92	10.89
Mg	1.65	28516.21	0.020	341.51	83.50
Ca	1.1	16092.53	0.0068	107.37	149.86
Sr	0.44	5754.67	0.0015	17.70	325.13
Zn	0.0044	57.43	0.0028	45.52	1.26
Cd	0.0095	133.96	0.00093	12.19	10.98
F^-	0.39	11461.87	0.035	646.06	17.74
Cl^-	0.285	5991.83	0.0095	172.79	34.68
Br^-	0.60	11788.85	0.0018	28.03	420.63
I^-	0.32	5799.83	0.00075	9.39	617.65
CH_4	0.52	2938.47	0.076	317.69	9.25
CF_4	0.17	707.94	0.034	115.32	6.14
CCl_4	0.14	613.89	0.0095	28.34	21.66
CBr_4	0.24	1055.82	0.0018	4.03	261.65
CI_4	0.16	631.25	0.00075	1.08	586.46
$FeCN_6^{4-}$	0.0072	6.34	0.0038	2.03	3.13
$RuCN_6^{4-}$	0.018	14.49	0.0011	0.70	20.58
Heme-CO	0.010	1.24	0.0038	0.34	3.66

Figure 7 and Table 1 show that computational efficiency is systematically improved by the use of ECP when the number of electronic shells is increased within a group. For representative elements, the overall improvement derived from pseudopotentials is usually between one and two orders of magnitude. In the case of transition elements, the speedup is substantially lower. To understand this different performance, it must be recalled that most representative elements pseudopotentials consider only the outermost electrons ($ns^j\ np^k$), but incorporate inner shells in the case of transition elements ($(n-1)s^2\ \ (n-1)p^6$).[30,36–39] For the iron atom, for example, this entails the explicit representation of $3s$ and $3p$ electrons, which are subject to a higher effective charge in comparison with the electrons in the third shell of the elements of the second row. Similarly, the ruthenium ECP incorporates $4s$ and $4p$ electrons to the valence charge. As a consequence, the speedup achieved from Fe and Ru

pseudopotentials is comparable to, or below that obtained for representative elements of the third and fourth row, respectively. The CRENBL Ar-like core pseudopotentials developed by Christiansen et al.,[33] consider only the ns^j and $(n-1)d^k$ electrons within the valence. The use of this ECP to propagate the electron dynamics of the $FeCN_6^{4-}$ complex leads to a 8-fold increase in performance with respect to the all-electron calculation, in contrast with the more modest speedup of 3× found for the CEP pseudopotential.

To close this section, we emphasize that the leap-frog Verlet integrator used in this work is a simpler and faster algorithm, but less stable, compared to the more sophisticated expansions typically employed in real time TDDFT simulations.[24] Thus, if the Verlet scheme is replaced by the Magnus propagator to evolve the electron dynamics of HCl with the ECP/6-31G** (valence only) basis, we find that the time-step can be risen from 0.015 au to 0.15 au. According to our tests, such an increase of an order of magnitude associated with the replacement of the leap-frog by the Magnus approach, appears to be a general result. In a similar way, the time-step to integrate the electronic degrees of freedom in C_2H_4 using the exponential midpoint method (EMM) reported by Wang et al. in all-electron Ehrenfest calculations with Gaussian basis sets,[8] is nearly five times larger than the one required by the Verlet propagation in our all-electron simulations for CH_4.

The maximum time-step is very sensitive to the specific basis-set and pseudopotential. For example, the CEP scheme with the corresponding basis set tolerates an integration time-step in HCl of about 2 au with the Magnus expansion. Comparable time-steps have been used with the Magnus propagator in SIESTA calculations,[18,19] where the quality of the numerical basis roughly pairs that of the CEP functions. In particular, a time-step as large as 1 au was reported in Fe-porphyrin calculations employing a Fe pseudopotential that describes explicitly only the 4s and 3d electrons.[19] Our calculations on the same system with the Magnus propagator and CEP, LANL2DZ or Stuttgart pseudopotentials, which take into account a more extended valence charge, including 3s, 3p, 4s, and 4p electrons, do not tolerate time-steps above 0.1 au (see Supporting Information). Another example of this

kind of behavior is presented in the Supporting Information for Zn: if it is modelled with just 4s electrons, a Magnus time-step of 2.4 au can be used, which drops to 0.005 au when the third shell is added to the valence. This explains the difference in time-steps across implementations.

4 Concluding remarks

This work implements effective core potentials in real time TDDFT simulations. It is shown that the use of pseudopotentials can have, in these kind of simulations, a much more significant impact on computational efficiency that it has in the case of SCF calculations. The reason for these substantial speedups, which may be as large as 600× for some representative elements, stems from the use of larger time-steps when the core charge, associated with high-frequency modes, is not evolved in time. Additionally, though with a lesser impact in most cases, the use of pseudopotentials reduces the dimension of the basis set and therefore cuts down the cost of matrix multiplication operations, which are at the core of the time-propagation algorithm. The use of a frozen-core approximation would provide the same gain in terms of time-step, but the dimension of the matrices will be no different from that in an all-electron calculation. Moreover, in contrast with the frozen-core scheme, pseudopotentials allow for the incorporation of relativsitic effects, and, with the appropriate choice of basis sets, the replacement of inner electrons by core potentials can be effected with practically no loss of accuracy.

In general terms, the speedup provided by a pseudopotential in the framework of electron dynamics, will depend on the angular momentum of the lower eigenstates in the valence, and on the effective charge. Thus, at variance with the trend expected in ground-state calculations, the overall gain in performance in transition elements with explicit inner electrons, turns out to be significantly below the one obtained in representative elements belonging to the same period, which have only the outermost electrons in the valence. For example, for

iron-containing compounds, the speedup is found to be around a factor of 3 or 4, while in the case of Br species, it is over two orders of magnitude. In any case, this study shows that the implementation of pseudopotentials makes a qualitative difference in the efficiency of real time TDDFT simulations, and appears to be an essential ingredient to tackle the quantum-dynamics of large chemical systems and nanostructures, with a much more significant impact than in ground-state electronic structure calculations with Gaussian-functions.

Acknowledgement

This research was supported by grants of the Universidad de Buenos Aires, UBACYT 20020130100097BA and Agencia Nacional de Promoción Científica y Tecnológica, PICT 2015-0672. Nicolás O. Foglia gratefully acknowledges CONICET for a doctoral fellowship, and Dr. Daisaku Ikeda and SGIAR for their support in his studies.

Supporting Information Available

The HCl molecule spectra obtained with various pseudopotentials in combination with the 6-311G** basis, and values of T_{max} corresponding to different pseudopotentials. This material is available free of charge via the Internet at `http://pubs.acs.org/`.

References

(1) Beratan, D.; Onuchic, J.; Winkler, J.; Gray, H. Electron–tunneling pathways in proteins. *Science* **1992**, *258*, 1740–1741.

(2) Nitzan, A.; Ratner, M. A. Electron Transport in Molecular Wire Junctions. *Science* **2003**, *300*, 1384–1389.

(3) Shah, A.; Adhikari, B.; Martic, S.; Munir, A.; Shahzad, S.; Ahmad, K.; Kraatz, H.-B. Electron transfer in peptides. *Chem. Soc. Rev.* **2015**, *44*, 1015–1027.

(4) Wang, L.; Long, R.; Prezhdo, O. V. Time-Domain Ab Initio Modeling of Photoinduced Dynamics at Nanoscale Interfaces. *Annu. Rev. Phys. Chem.* **2015**, *66*, 549–579.

(5) Kilina, S.; Kilin, D.; Tretiak, S. Light-Driven and Phonon-Assisted Dynamics in Organic and Semiconductor Nanostructures. *Chem. Rev.* **2015**, *115*, 5929–5978.

(6) Runge, E.; Gross, E. K. U. Density–Functional Theory for Time–Dependent Systems. *Phys. Rev. Lett.* **1984**, *52*, 997–1000.

(7) Lopata, K.; Govind, N. Modeling Fast Electron Dynamics with Real–Time Time–Dependent Density Functional Theory: Application to Small Molecules and Chromophores. *J. Chem. Theory Comput.* **2011**, *7*, 1344–1355.

(8) Wang, F.; Yam, C. Y.; Hu, L.; Chen, G. Time–dependent density functional theory based Ehrenfest dynamics. *J. Chem. Phys.* **2011**, *135*, 044126.

(9) Liang, W.; Chapman, C. T.; Li, X. Efficient first–principles electronic dynamics. *J. Chem. Phys.* **2011**, *134*, 184102.

(10) Tavernelli, I.; Röhrig, U. F.; Rothlisberger, U. Molecular dynamics in electronically excited states using time–dependent density functional theory. *Mol. Phys.* **2005**, *103*, 963–981.

(11) Theilhaber, J. *Ab initio* simulations of sodium using time-dependent density-functional theory. *Phys. Rev. B* **1992**, *46*, 12990–13003.

(12) Yabana, K.; Bertsch, G. F. Time–dependent local–density approximation in real time. *Phys. Rev. B* **1996**, *54*, 4484–4487.

(13) Krauss, M.; Stevens, W. J. Effective Potentials in Molecular Quantum Chemistry. *Annu. Rev. Phys. Chem.* **1984**, *35*, 357–385.

(14) Dolg, M.; Cao, X. Relativistic Pseudopotentials: Their Development and Scope of Applications. *Chem. Rev.* **2012**, *112*, 403–480.

(15) Kahn, L. R.; Baybutt, P.; Truhlar, D. G. *Abinitio* effective core potentials: Reduction of all–electron molecular structure calculations to calculations involving only valence electrons. *J. Chem. Phys.* **1976**, *65*, 3826–3853.

(16) Tavernelli, I. Electronic density response of liquid water using time-dependent density functional theory. *Phys. Rev. B* **2006**, *73*, 094204.

(17) Cheng, C.-L.; Evans, J. S.; Van Voorhis, T. Simulating molecular conductance using real–time density functional theory. *Phys. Rev. B* **2006**, *74*, 155112.

(18) Meng, S.; Kaxiras, E. Real-time, local basis-set implementation of time-dependent density functional theory for excited state dynamics simulations. *J. Chem. Phys.* **2008**, *129*, 054110–054110.

(19) Kolesov, G.; Grns, O.; Hoyt, R.; Vinichenko, D.; Kaxiras, E. Real-Time TD-DFT with Classical Ion Dynamics: Methodology and Applications. *J. Chem. Theory Comput.* **2016**, *12*, 466–476, PMID: 26680129.

(20) Ojanper, A.; Havu, V.; Lehtovaara, L.; Puska, M. Nonadiabatic Ehrenfest molecular dynamics within the projector augmented-wave method. *J. Chem. Phys.* **2012**, *136*.

(21) Andrade, X.; Strubbe, D.; De Giovannini, U.; Larsen, A. H.; Oliveira, M. J. T.; Alberdi-Rodriguez, J.; Varas, A.; Theophilou, I.; Helbig, N.; Verstraete, M. J.; Stella, L.; Nogueira, F.; Aspuru-Guzik, A.; Castro, A.; Marques, M. A. L.; Rubio, A. Real-space grids and the Octopus code as tools for the development of new simulation approaches for electronic systems. *Phys. Chem. Chem. Phys.* **2015**, *17*, 31371–31396.

(22) Nitsche, M. A.; Ferreria, M.; Mocskos, E. E.; Lebrero, M. C. G. GPU Accelerated

Implementation of Density Functional Theory for Hybrid QM/MM Simulations. *J. Chem. Theory Comput.* **2014**, *10*, 959–967.

(23) Morzan, U. N.; Ramírez, F. F.; Oviedo, M. B.; Sánchez, C. G.; Scherlis, D. A.; Lebrero, M. C. G. Electron dynamics in complex environments with real–time time dependent density functional theory in a QM–MM framework. *J. Chem. Phys.* **2014**, *140*, 164105.

(24) Castro, A.; Marques, M. A. L.; Rubio, A. Propagators for the time-dependent Kohn-Sham equations. *The Journal of Chemical Physics* **2004**, *121*.

(25) Shin, D.; Lee, G.; Miyamoto, Y.; Park, N.

(26) Perdew, J. P.; Burke, K.; Ernzerhof, M. Generalized Gradient Approximation Made Simple. *Phys. Rev. Lett.* **1996**, *77*, 3865–3868.

(27) Perdew, J. P.; Burke, K.; Ernzerhof, M. Generalized Gradient Approximation Made Simple Phys. Rev. Lett. 77, 3865 (1996). *Phys. Rev. Lett.* **1997**, *78*, 1396–1396.

(28) Cuevasanta, E.; Zeida, A.; Carballal, S.; Wedmann, R.; Morzan, U. N.; Trujillo, M.; Radi, R.; Estrin, D. A.; Filipovic, M. R.; Alvarez, B. Insights into the mechanism of the reaction between hydrogen sulfide and peroxynitrite. *Free Radical Bio. Med.* **2015**, *80*, 93 – 100.

(29) Stevens, W. J.; Basch, H.; Krauss, M. Compact effective potentials and efficient shared–exponent basis sets for the first–and second–row atoms. *J. Chem. Phys.* **1984**, *81*, 6026–6033.

(30) Stevens, W. J.; Krauss, M.; Basch, H.; Jasien, P. G. Relativistic compact effective potentials and efficient, shared–exponent basis sets for the third–, fourth–, and fifth–row atoms. *Can. J. Chemistry* **1992**, *70*, 612–630.

(31) Cundari, T. R.; Stevens, W. J. Effective core potential methods for the lanthanides. *J. Chem. Phys.* **1993**, *98*, 5555–5565.

(32) Fernandez Pacios, L.; Christiansen, P. A. *Abinitio* relativistic effective potentials with spin–orbit operators. I. Li through Ar. *J. Chem. Phys.* **1985**, *82*, 2664–2671.

(33) Hurley, M. M.; Pacios, L. F.; Christiansen, P. A.; Ross, R. B.; Ermler, W. C. Abinitio relativistic effective potentials with spin–orbit operators. II. K through Kr. *J. Chem. Phys.* **1986**, *84*, 6840–6853.

(34) LaJohn, L. A.; Christiansen, P. A.; Ross, R. B.; Atashroo, T.; Ermler, W. C. *Abinitio* relativistic effective potentials with spin–orbit operators. III. Rb through Xe. *J. Chem. Phys.* **1987**, *87*, 2812–2824.

(35) Ross, R. B.; Powers, J. M.; Atashroo, T.; Ermler, W. C.; LaJohn, L. A.; Christiansen, P. A. *Abinitio* relativistic effective potentials with spin–orbit operators. IV. Cs through Rn. *J. Chem. Phys.* **1990**, *93*, 6654–6670.

(36) Hay, P. J.; Wadt, W. R. *Abinitio* effective core potentials for molecular calculations. Potentials for the transition metal atoms Sc to Hg. *J. Chem. Phys.* **1985**, *82*, 270–283.

(37) Wadt, W. R.; Hay, P. J. *Abinitio* effective core potentials for molecular calculations. Potentials for main group elements Na to Bi. *J. Chem. Phys.* **1985**, *82*, 284–298.

(38) Hay, P. J.; Wadt, W. R. *Abinitio* effective core potentials for molecular calculations. Potentials for K to Au including the outermost core orbitals. *J. Chem. Phys.* **1985**, *82*, 299–310.

(39) Dolg, M.; Wedig, U.; Stoll, H.; Preuss, H. Energy–adjusted *abinitio* pseudopotentials for the first row transition elements. *J. Chem. Phys.* **1987**, *86*, 866–872.

(40) Bode, B. M.; Gordon, M. S. Fast computation of analytical second derivatives with

effective core potentials: Application to Si_8C_{12},Ge_8C_{12}, and Sn_8C_{12}. *J. Chem. Phys.* **1999**, *111*, 8778–8784.

(41) Myer, J. A.; Samson, J. A. R. Vacuum–Ultraviolet Absorption Cross Sections of CO, HCl, and ICN between 1050 and 2100 . *J. Chem. Phys.* **1970**, *52*, 266–271.

(42) Nee, J. B.; Suto, M.; Lee, L. C. Quantitative photoabsorption and fluorescence study of HCl in vacuum ultraviolet. *J. Chem. Phys.* **1986**, *85*, 719–724.

(43) Krishnan, R.; Binkley, J. S.; Seeger, R.; Pople, J. A. Self–consistent molecular orbital methods. XX. A basis set for correlated wave functions. *J. Chem. Phys.* **1980**, *72*, 650–654.

(44) McLean, A. D.; Chandler, G. S. Contracted Gaussian basis sets for molecular calculations. I. Second row atoms, Z=11–18. *J. Chem. Phys.* **1980**, *72*, 5639–5648.

(45) Labello, N. P.; Ferreira, A. M.; Kurtz, H. A. Correlated, relativistic, and basis set limit molecular polarizability calculations to evaluate an augmented effective core potential basis set. *Int. J. Quantum Chem.* **2006**, *106*, 3140–3148.

(46) EMSL Basis Set Exchange. `https://bse.pnl.gov`, Accessed: 2016-01-30.

(47) Godbout, N.; Salahub, D. R.; Andzelm, J.; Wimmer, E. Optimization of Gaussian–type basis sets for local spin density functional calculations. Part I. Boron through neon, optimization technique and validation. *Can. J. Chemistry* **1992**, *70*, 560–571.

For table of contents use only

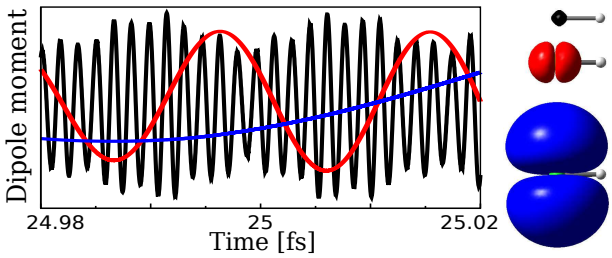

Title: The role of core electrons in quantum dynamics using TDDFT

Authors: Nicolás O. Foglia, Uriel N. Morzan, Dario A. Estrin, Damian A. Scherlis, Mariano C. Gonzalez Lebrero